Acta Biomaterialia 107 (2020) 194–203

Contents lists available at ScienceDirect

Acta Biomaterialia

journal homepage: www.elsevier.com/locate/actbio

Full length article

The multiscale hierarchical structure of *Heloderma suspectum* osteoderms and their mechanical properties

Francesco Iacoviello[a], Alexander C. Kirby[b], Yousef Javanmardi[c], Emad Moeendarbary[c,d], Murad Shabanli[c], Elena Tsolaki[b], Alana C. Sharp[e], Matthew J. Hayes[f], Kerda Keevend[g], Jian-Hao Li[g], Daniel J.L. Brett[a], Paul R. Shearing[a], Alessandro Olivo[b], Inge K. Herrmann[g], Susan E. Evans[e], Mehran Moazen[c], Sergio Bertazzo[b,*]

[a] *Electrochemical Innovation Lab, Department of Chemical Engineering, University College London, London WC1E 7JE, UK*
[b] *Department of Medical Physics and Biomedical Engineering, University College London, London WC1E 6BT, UK*
[c] *Department of Mechanical Engineering, University College London, London WC1E 7JE, UK*
[d] *Department of Biological Engineering, Massachusetts Institute of Technology, Cambridge, MA, 02139, USA*
[e] *Department of Cell and Developmental Biology, University College London, London WC1E 6BT, UK*
[f] *Department of Ophthalmology, University College London, London WC1E 6BT, UK*
[g] *Department of Materials, Meet Life, Swiss Federal Laboratories for Materials Science and Technology, (Empa), Lerchenfeldstrasse 5, CH-9014 St. Gallen, Switzerland*

ARTICLE INFO

Article history:
Received 19 November 2019
Revised 13 February 2020
Accepted 18 February 2020
Available online 25 February 2020

Keywords:
Biomineralizations
Osteoderms
Lizards
Bones
Armour plates

ABSTRACT

Osteoderms are hard tissues embedded in the dermis of vertebrates and have been suggested to be formed from several different mineralized regions. However, their nano architecture and micro mechanical properties had not been fully characterized. Here, using electron microscopy, μ-CT, atomic force microscopy and finite element simulation, an in-depth characterization of osteoderms from the lizard *Heloderma suspectum*, is presented. Results show that osteoderms are made of three different mineralized regions: a dense apex, a fibre-enforced region comprising the majority of the osteoderm, and a bone-like region surrounding the vasculature. The dense apex is stiff, the fibre-enforced region is flexible and the mechanical properties of the bone-like region fall somewhere between the other two regions. Our finite element analyses suggest that when combined into the osteoderm structure, the distinct tissue regions are able to shield the body of the animal by bearing the external forces. These findings reveal the structure-function relationship of the *Heloderma suspectum* osteoderm in unprecedented detail.

Statement of Significance

The structures of bone and teeth have been thoroughly investigated. They provide a basis not only for understanding the mechanical properties and functions of these hard tissues, but also for the *de novo* design of composite materials. Osteoderms, however, are hard tissues that must possess mechanical properties distinct from teeth and bone to function as a protective armour. Here we provide a detailed analysis of the nanostructure of vertebrate osteoderms from *Heloderma suspectum*, and show that their mechanical properties are determined by their multiscale hierarchical tissue. We believe this study contributes to advance the current knowledge of the structure-function relationship of the hierarchical structures in the *Heloderma suspectum* osteoderm. This knowledge might in turn provide a source of inspiration for the design of bioinspired and biomimetic materials.

* Corresponding author.
E-mail address: s.bertazzo@ucl.ac.uk (S. Bertazzo).

https://doi.org/10.1016/j.actbio.2020.02.029

1. Introduction

Amongst tetrapods, turtles [1,2], alligators [3–5], frogs [6], lizards [5,7,8], and mammals [5,9] possess hard tissue in their skin called osteoderms [4,10,11]. Osteoderms are found in the skin as part of an integumentary skeleton [5,11] and can be presented in several different shapes and sizes [5,12,13]. Like bones and teeth, osteoderms are composed of calcium phosphate and organic components (mainly collagen) [3,5]. Osteoderms are generally considered to provide protection in the same way as an armour, but other functions have been proposed, including thermal regulation [14–19], ion storage (calcium) [20], and locomotion [21]. As a consequence of their widespread occurrence and different proposed functions, the mechanical properties [1,4,22–24], morphology [1,5,7,9–12,24–30] and histology [5,7,9,26–28,30] of osteoderms have been widely studied.

Based on these previous work, and also on the wide diversity in osteoderm morphology across animal species, we hypothesized that the composition and ultrastructure of osteoderms would differ from those of other hard tissues, such as bone and teeth. Moreover, based on previous work showing that osteoderms from different animals were composed of different regions [7,11,27,31], we also hypothesized that these regions would present different nanostructures and that the precise arrangement of these regions would be relevant to its macroscopic mechanical behaviour and function.

Osteoderms are particularly common and diverse in lizards [5], where their shapes, range from compound plates, and scales [5,32] to needles [33]. They also vary in size from centimeters to millimeters [26,34], but size is not always correlated with body length and it is not uncommon for small lizards to present large osteoderms [35].

Helodermatidae (Fig. 1(a)) is a family of venomous lizards that has osteoderms distributed over the entire body (Fig. 1(b), CT-scan of the head of *Heloderma suspectum*, as example to visualization of distribution of osteoderms on the animal skin). The morphology of individual osteoderms falls between scales and needles [12]. Each osteoderm has a large base (Fig. 1(c), blue region) that is embedded in the dermis of the skin, and a high-density region (Fig. 1(c), orange region) that is shaped into spikes that project into the epidermis.

The size and shape of helodermatid osteoderms make them an ideal candidate for an initial characterization of the nano and ultrastructure of the different tissues that form osteoderms in lizards. It also allows testing of the potential contributions made by different nanostructures to the overall mechanical properties of lizard osteoderms.

Here we present a detailed characterization of the nano and ultrastructure of *Heloderma suspectum* osteoderms, as well as their mechanical properties using electron microscopy, μ-CT, atomic force microscopy, and finite element analysis. Our results show that the these osteoderms are indeed formed from unique hard tissues, with a nano and ultrastructure that is different from bones and teeth. We also demonstrate how the mechanical properties and distribution of the different regions within these osteoderms combine to maximize their efficiency as a load bearing armour.

2. Materials and methods

2.1. Sample collection

Lizard skin samples from 4 different animals were obtained from lizards donated to the Evans lab (UCL) by the Pathology Department, Zoological Society of London. The skin samples were taken from animals that had been frozen upon receipt**.** Subsamples were then obtained from different regions of each animal's skin. After dissection, samples were fixed as described in session 2.2. Embedding was done no later than 2 h following dissection. All samples were obtained form adult animals.

2.2. Dehydration and resin embedding

Lizard skin samples were fixed with 1% glutaraldehyde for 15 min, then dehydrated by submerging in an ethanol/distilled water series of gradients 20, 30, 40, 50, 60, 70, 80, 90, 100%, for 1 h each. Samples were then infiltrated with "EMbed 812" (EMS) epoxy resin diluted with absolute ethanol in the ratios 3 ethanol:1 resin, 2:1, 1:1, 1:2, 1:3, then 100% epoxy resin, for 4 h at each concentration, overnight at 1:1. Samples were then cured by heating at 60 °C for 48 h; after solidifying, the resin blocks were cut into 1 mm thick sections, using a Buehler Isomet low speed saw. These were then water-polished, using sand paper with a grit series of 1250, 2500 and 5000, and a Buehler MetaServ 250 grinder-polisher for 5–10 min per grade at 250 RPM. Next, polishing diamond compounds with 3 μm, 1 μm and finally 0.25 μm diameter bead size were used to polish samples at 250 RPM, for 5–10 min.

2.3. Scanning electron microscopy (SEM)

Cut and polished sections were attached to SEM specimen stubs with carbon tape, or carbon paste, then coated with carbon using a Quorum K975X Carbon coater, painted with silver paint and imaged using a Zeiss Sigma VP scanning electron microscope at 10–20 kV, aperture of 30 μm, working distance 9–11 mm, and back-scattered electron detector (BSE). Secondary electron and in-lens detector were also used, and these were combined within the same image for red/green stacked density dependent images. Additionally, a Hitachi S-3400 N scanning electron microscope with an incorporated Oxford Instruments EDX detector, using a voltage of 10 kV, aperture of 30 mm and a working distance of 10 mm was used. BSE detectors allowed the visualization of the relative density of minerals in the sample. An Energy Dispersive X-ray (EDX) function was used for elemental mapping of the mineralisation sites. For all analyses, an accelerating voltage of 10 kV was

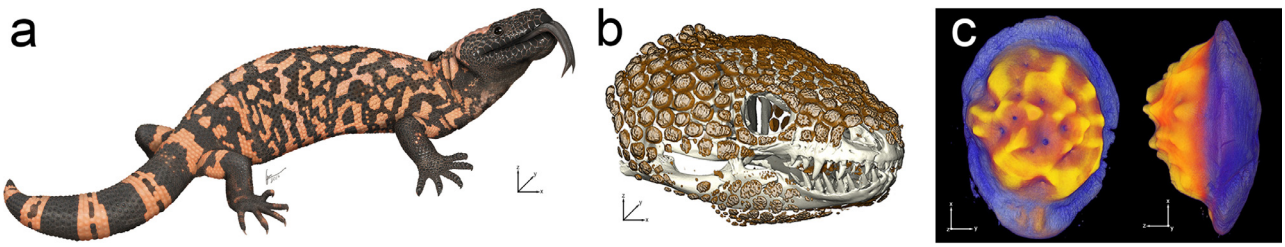

Fig. 1. Structure and composition of the osteoderms of *Heloderma suspectum* (Gila Monster). (a) Whole-body illustration of *Heloderma suspectum*. (b) Reconstructed macro-CT scan of *Heloderma suspectum* cranium and overlying osteoderms. (c) Reconstructed micro-CT scan of a single *Heloderma suspectum* osteoderm, depicting two regions of different density (orange and blue). (For interpretation of the references to colour in this figure legend, the reader is referred to the web version of this article.)

used, with working distance of 7–10 mm. For the EDX analyses, INCA Energy Software with acquisition time of 15–25 s was used.

2.4. Atomic force microscopy (AFM)

A JPK AFM Nanowizard Cellhesion 200 (JPK Instruments AG, Berlin, Germany) interfaced with a motorized XY stage was used to conduct nano-indentation measurements and extract stiffness maps. A stiff cantilever with a sharp tip (RTESPA-525, Bruker, nominal spring constant of 200 N/m) was used. Exact cantilever spring constant was determined using a direct method of a reference cantilever. The AFM setup was mounted on an Olympus inverted microscope and a CCD camera allowed monitoring of the position of the cantilever over defined regions of the sample. Force-distance curves were taken with an approach speed of 2 µm/s and a set force of 200 µN by an automated raster scan using a motorized stage with 10 µm step size. Prior to indentation tests, the sensitivity of the cantilever was set by measuring the slope of a force-distance curve acquired on Sapphire substrate (PFQNM-SMPKIT-12 M kit, Bruker). Using JPK Data Processing software, the contact point was found. The stiffness values Stiffness=$E/(1-\upsilon^2)$ were extracted from the force-distance curves by fitting the contact portion of curves to a Hertz contact model between a sharp triangular tip and an infinite half space, where E is the elastic modulus and υ the Poisson ratio as previously demonstrated in literature [36].

2.5. Finite element simulations

A commercial finite element (FE) software (ANSYS R19, Ansys Inc.) was used to simulate the mechanical response of the osteoderm segments against applied forces and displacements. The complex geometry of the osteoderm consists of four regions: vasculature, bone, fibre region and dense region, each with distinct mechanical characteristics as measured via AFM indentation tests. The geometry of these segments, reconstructed from CT scan images, was exported to ANSYS. Three-dimensional 4-node solid elements were employed to discretise the domain were exported to ANSYS. Three-dimensional 4-node solid elements were employed to discretise the domain. To determine the appropriate mesh size, a mesh sensitivity analysis was carried out considering ~25,000 to ~1,000,000 elements. The results demonstrated that ~400,000 elements are sufficiently accurate. A linear elastic isotropic constitutive model was employed to describe the mechanical behaviour of the four segments in the model, with stiffness values obtained from AFM indentation tests with Poisson's ratio of 0.3. To apply the boundary conditions, all of the surface nodes located on the 250 µm of the lower part of the osteoderm were constrained in all directions. For the stress control problem, a uniformly distributed load with a total magnitude of 3.45 N were applied to all nodes located on the upper 250 µm surface of the osteoderm. For the deformation control problem, a constant displacement (with total magnitude of around 0.8% of the height of the osteoderm) was applied to the same nodes. Finally, the built in ANSYS solver was employed to obtain the distribution of stress or strain within the domain.

2.6. Focused ion beam (FIB)/transmission electron microscopy (TEM)

Samples were silver painted and carbon coated using a Quorum K975X Carbon coater. For sample preparation, a FEI Helios NanoLab 600 DualBeam Focused Ion Beam System, at Imperial College London, was used. A micro region of each sample was coated with a Platinum layer at 30 kV and 93 pA. Following that, currents between 93 pA and 2.8 nA were used for section lift out and thinning of the sample to 100 nm. The sample was then placed on a carbon grid and transferred to a JEOL JEM 2100 Plus Transmission Electron Microscope at Imperial College London, to be imaged using 200 kV and 120 kV. Selected-area electron diffraction (SAED) was done at 200 kV. Image analysis was performed on ImageJ software.

2.7. Raman spectroscopy

Raman imaging was performed using a confocal Raman microscope (alpha 300R, WITec, Ulm, Germany). Spectra were collected using a 532 nm laser and a 50x (0.55NA) LD objective. A 600 lines per mm spectral grating was used (UHTS 300, WITec, Ulm, Germany). Maps were acquired using 1 µm step size and an integration time of 2 s.

2.8. Spectral analysis

Raw Raman spectra in the 1800–700 cm^{-1} region were extracted and pre-processed (MATLAB, The MathWorks Inc.) for corrupt signal removal, baseline correction, and Savitzky–Golay (SG) smoothing. The 2nd derivative spectra, derived from the SG smoothing, were then vector normalized independently in the 1800–1380 cm^{-1}, 1380–1120 cm^{-1}, and 1120–700 cm^{-1} regions, before being used in hierarchical cluster analysis (HCA) and principal component analysis (PCA). The spectral information of each spectrum is represented by 435 wavenumber-magnitude pairs, uniformly covering 1800–700 cm^{-1}. In the HCA step, the spectra were divided into 3 clusters based on Ward's algorithm. In addition to plotting the spatial distribution of these clusters, a PCA scores plot was produced to visualize the distribution of each cluster in the PC space. Average spectrum of each cluster was computed to demonstrate each individual cluster's spectral features. Spectra of reference for collagen (keratin) samples were used to identify clusters of collagen (keratin) constituents. Two-sample t-tests were conducted between the 2nd derivative spectra (for all 435 wavenumbers) of the two clusters.

2.9. Polarised light microscopy

Samples were embedded in Araldite M (Agar Scientific). The resulting resin block was cut to 650 nm sections on a Leica Reichert Ultracut S Microtome with a glass knife. Sections were collected on glass slides, stained with 0.5% aqueous toluidine blue on a heating block at 70 °C for 15 s and washed with 70% ethanol. The resultant metachromatic stain was observed through bipolarised light on a 510 Zeiss LSM 510 Meta Confocal Laser scanning microscope at 10x and 20x magnifications. 20x magnification images were stitched together in Photoshop CS6 (Abode) and then cropped.

2.10. X-ray computed tomography (X-ray CT)

The whole head of the *Heloderma suspectum* was dissected from the body at the base of the skull, wrapped in Parafilm and imaged directly in a Nikon XT H 225 scanner (macro-CT, Nikon Metrology, Tring, UK). Osteoderm samples were dissected and washed 5 times in ddH_2O then 5 times in 70% ethanol and left to dry for 48 h. The non-mineralised soft tissue was removed using a scalpel blade. An A Series Compact LASER micromachining system (Oxford Laser, Oxford, UK) was used to cut out a cylinder 1 mm wide. This cylinder was then cut to incrementally smaller cylinders of 500 µm diameter, then 100 µm diameter, then finally 65 µm in diameter. The thinner, upper part of this series of cylinders was imaged using either a ZEISS Xradia 520 Versa (micro-CT, 500 and 100 µm diameter cylinders) or a ZEISS Ultra 810 X-ray (nano-CT, 65 µm cylinder) microscopes (Carl Zeiss X-ray Microscopy Inc., Pleasanton, CA). The raw transmission images from the three X-ray CT imaging experiments were reconstructed using commercial image reconstruction

software packages (Zeiss XMReconstructor, Carl Zeiss X-ray Microscopy Inc., Pleasanton, CA, and CT Pro 3D, Nikon Metrology, Tring, UK), which employ a filtered back-projection algorithm. The 3D reconstructed volumes of the samples were segmented and analysed using Software Avizo Fire 9.2 (Thermo Fisher Scientific, USA).

2.11. Histology

Dissected samples measuring no more than $2cm^3$ were fixed in formalin at 4% concentration in Phosphate Buffered Saline, then placed in decalcification solution (1.9% Glutaraldehyde, 0.15 M EDTA, in 0.06 M sodium cacodylate buffer, adj 7.4 pH) at 4°C, changing to fresh solution every 7 days, for one month. The samples were then washed in distilled water, embedded in paraffin wax and cut with a microtome to 5 µm thick sections. These sections were then stained with both Haematoxylin and Eosin, Alcian Blue, Masson's Trichrome or Elastic Van Gieson stains and were scanned using a Leica SCN400 scanner.

3. Results

X-ray Computed tomography (X-ray CT) scanning and scanning electron microscopy (SEM) show that each osteoderm can be divided into four structurally distinct regions (Fig. 2(a) and Supplementary Fig. S1, the same regions have been found on osteoderms from all parts of the animal body, Supplementary Fig. S2): a mineralized region (I) displaying cells and a bone-like morphology (Fig. 2(a) and (b)), which is adjacent to a region (II) composed of cells and regularly interspaced fibre bundles that weave into a mineralized matrix (Fig. 2(a) and (c)). These two regions are capped by a third mineralized region (III), which is poorly cellularized (Fig. 2(a) and (d)) and contains micro- and nanofibres surrounded by a dense mineralized matrix. These three mineralized regions are arranged around a non-mineralized vascular lumen (region IV) [37] (Fig. 2(a) and Supplementary Fig. S3). [38]

Histological slides of osteoderms embedded in araldite and stained with toluidine blue were imaged in optical microscopes to determine the orientation of collagen fibres in the different regions and whether this is related to the collagen fibres present in the soft tissue surrounding the osteoderm. The micrographs show that the collagen fibres present in the osteoderms do indeed present the same orientation as those in the collagen forming the surrounding tissue (as demonstrated by the blue and orange colours that indicate the orientation of fibres). Also, several of these fibres apparently cross over from the soft tissue into the osteoderm (Fig. 3).

Optical micrographs were acquired in order to evaluate the organic composition of histological sections of a demineralized osteoderm stained with Masson's Trichrome [39]. These micrographs suggest the presence of collagen in regions I and II, but not in region III (Fig. 4(a)). Histological staining also suggests the presence of keratin at the base of the fibre-enforced mineralized region II. To confirm the possible presence of keratin at the base of the osteoderm histological slides were analysed by Raman spectroscopy. Raman spectral signatures show similarities in the C–H stretch and the amide I band [40] between the keratin-rich top layer and the osteoderm base (Fig. 4(b), Supplementary Fig. S4). Hierarchical cluster analysis (HCA) and principal component analysis (PCA) (Fig. 4(c), Supplementary Fig. S4) further indicate the presence of keratin or keratin-like deposits at the base of the osteoderm.

To evaluate the microstructure of the different regions present in the *Heloderma suspectum* osteoderm, µ-CT scans were carried out in regions I, II and III. At the microscale, the spatial distribution, 3D organization and size of organic fibres, as well as the cell and mineral distribution, differ in the three mineralized regions (Fig. 5).

To evaluate the nano structure of the three regions, FIB and TEM were acquired. In region I, the spatial distribution of collagen fibres (Fig. 6(a) and (d)) and crystallinity resemble those of bone (Fig. 6(d) inset) [41,42]. Region II in contrast to region I, presents regularly interspaced bundles of non or poorly mineralized collagen fibres (Fig. 6(b)) with an average diameter of 15 µm (collagen is confirmed by the characteristic 67 nm banding (Fig. 6(b))). In addition, focused ion beam (FIB) sections (Fig. 6(b)) show the presence of dense mineralized spherical nanoparticles in region II (Fig. 6(b)). Transmission electron micrographs (TEM) confirm that these spherical particles (Fig. 6(e)) are formed from lines of crystals spaced by 10 nm. Moreover, selective area electron diffraction (SAED) demonstrates that the minerals in the spherical particles have higher crystallinity and crystal orientation than the surrounding structures (Fig. 6(e) insets). Region III displays microfibres, but no cells in the mineralized matrix (Fig. 6(c)). Region III is formed from two distinct types of organic fibres, as confirmed by FIB and TEM. These fibres have diameters of 200 nm and 5 nm, respectively, and are embedded in a highly crystalline mineralized matrix (Fig. 6(c) and (f) – with full width half maximum (FWHM) obtained from the SAED of 4 arbitrary units (a.u.) compared to 14 a.u. of the bone region, 10 a.u. of the mineralized fibres and 19 a.u of the dense mineralized spherical particles).

To investigate the mechanical properties of osteoderms, we performed nano-indentation tests using an atomic force microscope (AFM) to evaluate the stiffness of each of the three mineralized regions (Fig. 7). The indentation experiments were performed in two animal samples. On each sample, we created three maps at the regions indicated in Fig. 7(a). Each stiffness map contains at least 100 indentation measurement points and the presented box plot is the combined results of the maps from the two samples (Fig. 7(b)). Region III is the stiffest material in the osteoderm, followed by regions I and II respectively (Fig. 7(b)). As expected, region I has similar stiffness (13 ± 6 GPa) to bone [43], whereas region III has a stiffness (21 ± 6 GPa) value similar to that of dentin [44]. Interestingly, the measured stiffness of region II (3 ± 2 GPa) is distinct from any value previously reported in mineralised vertebrate tissues [22].

To simulate the mechanical behaviour of the whole osteoderm structure which contains all three mineralized regions (I, II, III) and the non-mineralized region (IV), we used the stiffness values obtained from the nano-indentation measurements (Fig. 7) for a finite element (FE) analysis. This setup allowed us to simulate the stress and strain distribution under application of different loading conditions.

Initially, a full osteoderm was µ-CT scanned and then reconstructed. We used the osteoderm reconstruction to assess four different scenarios (Fig. 8(a)): in the first three scenarios, the osteoderm is considered to be homogeneously formed from only one of the mineralized regions (Fig. 8(a) I, II, III), and in the fourth scenario, the osteoderm contains all four regions, resembling the actual osteoderm architecture (Fig. 8(a) IV). Using this setup, strain and stress generated by the four model osteoderms in response to external force and deformation can be computed by applying a uniform load (Fig. 8(b)) or uniform displacement (Fig. 8(c)) to the upper surface of each model osteoderm, while constraining the lower surface in all directions. External displacement of the osteoderm formed from regions I or III causes the generation of large stresses within the osteoderm (Fig. 8(c) I and III). In the osteoderm formed from region II, application of external force leads to the development of large strains (Fig. 8(b) II). However, the model containing all four regions leads to substantially lower levels of stress (2- to 3-fold less stress, compared to the models composed of only region I or III, Fig. 8(c) IV) and strain

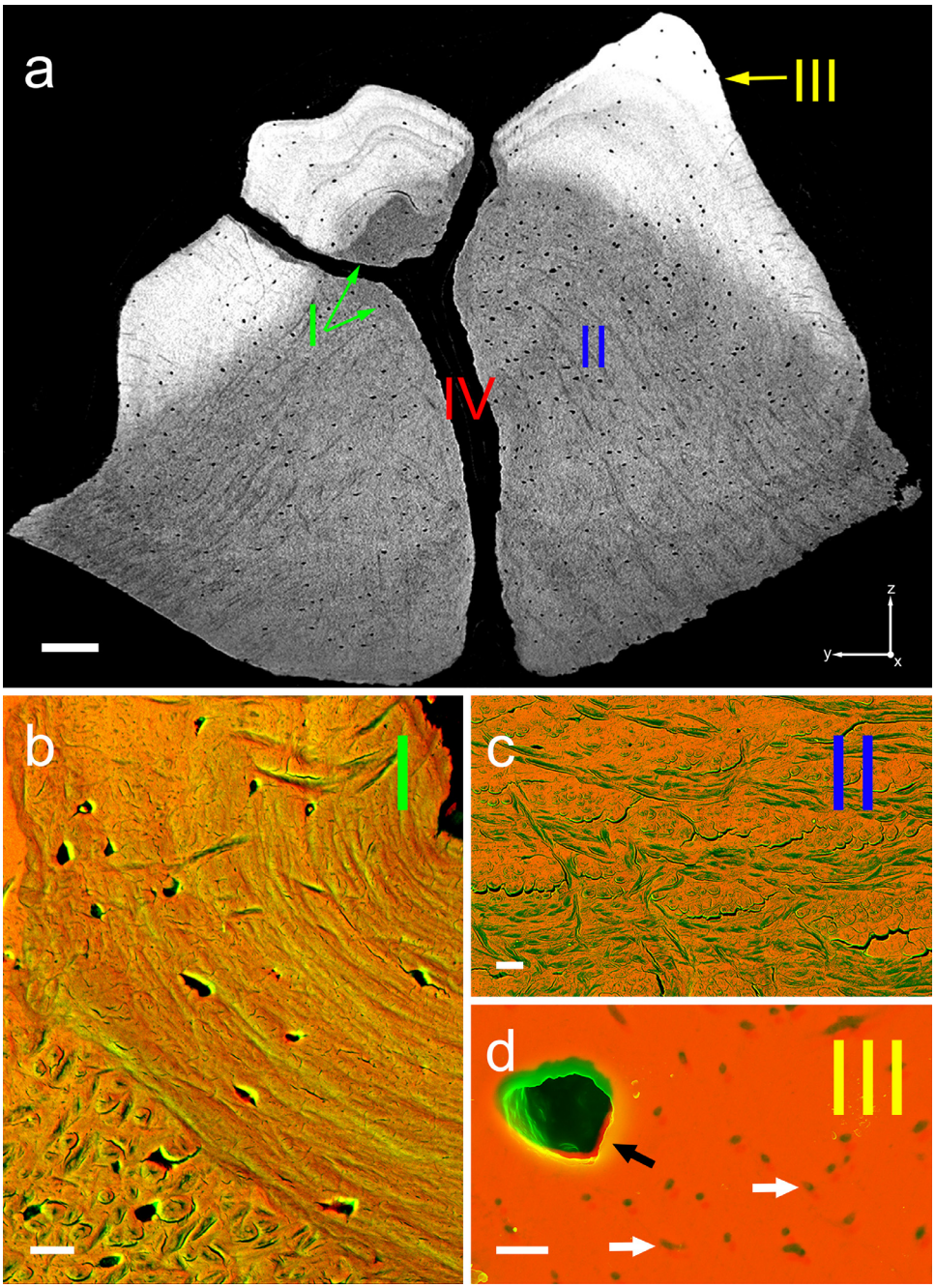

Fig. 2. Micro structure of osteoderm of *Heloderma suspectum*. (a) Micro-CT scan of transversal section of a single *Heloderma suspectum* osteoderm. Scale bar = 100 µm. (b) Density-dependent colour scanning electron micrograph (DDC-SEM) [38] of region I, with organic material in green and mineral in orange. Scale bar = 100 µm. (c) DDC-SEM of region II, with organic material in green and mineral in orange. Scale bar = 100 µm. (d) DDC-SEM of region III, with organic material in green and mineral in orange. Scale bar = 100 µm. (For interpretation of the references to colour in this figure legend, the reader is referred to the web version of this article.)

(1.6 times lower, compared to the model composed of region II, Fig. 8(b) IV).

4. Discussion

As previously reported, osteoderms are formed from different mineralized regions [7,11,27,31], and our µ-CT scan, combined with SEM results of a single osteoderm from *Heloderma suspectum*, clearly demonstrated that these different mineralized regions have distinct densities and distinct micro-architecture (Fig. 2). In literature, even when studies on osteoderms reported different regions [7,11,27,31], to the best of our knowledge, they did not identify three different calcified regions, but rather only two regions. In that case, one was the osteodermine [7,31] and the other region was described as woven fibrous bone [7]. Our results indicate that the calcified regions I and II might have been mistaken for one, due to the low resolution of the methods previously available. Indeed, we applied the same methods to osteoderms from other lizards and found similar microstructures on different lizard families (Supplementary Fig. S5 and S6).

The clear difference in micro architecture between the three regions potentially indicates they might each have their own mechanism of formation. It might also mean that these different regions could contribute to distinct mechanical properties towards the overall function of the osteoderm as a form of protection. In particular, the fibrous region (region II) are quite distinct from the

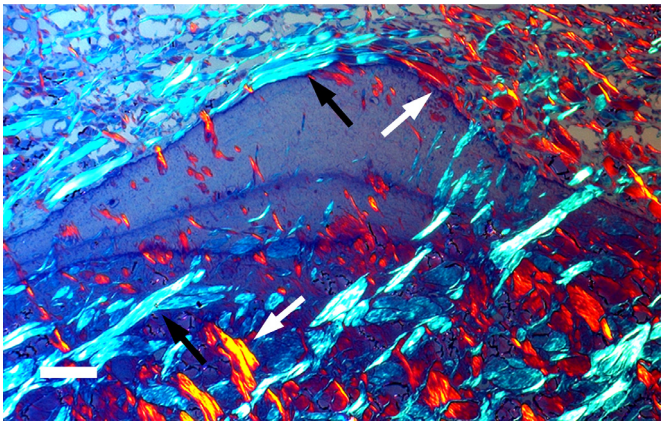

Fig. 3. Polarized optical micrograph of araldite section of osteoderm, stained with Toluidine blue. Black arrows indicate blue fibres oriented in one direction, whereas white arrows show orange fibres orientated at 90° in relation to the fibres in blue. Scale bar = 50 µm. (For interpretation of the references to colour in this figure legend, the reader is referred to the web version of this article.)

other regions. It is interesting how several of the collagen fibre bundles are found across the whole of the osteoderm (Fig. 3) and some even protrude into the surrounding tissue. Indeed, these are virtually indistinguishable from the collagen fibres present in the surrounding soft tissue. These collagen bundles can be found in all regions, and with the same orientation as the fibres observed in the surrounding tissue. This can be clearly seen on polarized micrographs (Fig. 3), which supports a potential correlation between the collagen present in the osteoderm and the collagen present in the surrounding tissue, as has been previously suggested in the literature [7].

The histological micrographs present results for the organic composition of which are similar to those reported in the literature for other osteoderms [5,7,35], with the upper region having no collagen, the middle portion presenting a considerable amount of collagen and the lower region being stained with some degree of what could be keratin. The presence of keratin is then confirmed by Raman spectroscopy. This is particularly interesting as keratin is usually not part of vertebrate hard tissues, providing evidence for the unique composition of osteoderm compared to other hard tissues, such as bone or teeth. To the best of our knowledge, the only other known hard tissue to contain keratin is baleen [45]. In addition to collagen and keratin, PCA also suggests the presence of glycogen, which has previously been reported in osteoderms [25].

With the microstructure and organic composition results at hand, we decided to evaluate the nano and ultrastructure of the calcified regions. The µ-CT scans (Fig 5) we acquired support our SEM analysis, clearly demonstrating that the nano architecture of the different regions is considerably different in relation to the distribution of cells, the collagen fibres and other organic fibres. The µ-CT scans of the bone-like region (region I) do not show the collagen fibres that could be visualized by FIB-TEM analysis (Fig 6), and therefore present the typical ultrastructure that is found in bone. The fibrous region (region II) presents an intricate organization of a bunch of fibres (Fig. 5) that are laid across the mineralized region. By FIB-TEM, however, it is clear that these bunches of fibres are formed from collagen fibres that combined into a bunch of around 15 µm of diameter. To the best of our knowledge, this is the first time that this kind of organization is described in a calcified tissue. In the literature similar regions can be observed on histological slides [5,7,35] and have been suggested to be formed by woven bone [7], a fair assumption, since histology would stain in the same way as bone, and the nano architecture can be only demonstrated by fully calcified sections sectioned by FIB-TEM analysis.

Finally, the top dense region (region III) is an interesting case, since it presents a very dense calcified structure, with few cells but with organic fibres (Fig. 5) distributed along the calcified matrix. FIB-TEM analysis (Fig. 6) shows that the fibres observed on µ-CT scans do not present typical collagen bands, a suggestion that these fibres are not collagen. Moreover, the same method confirms our SEM results, showing the presence of nano fibres other than the micro fibres distributed in the calcified matrix. The identity and function of these fibres is still elusive, but future research using biochemical methods could identify their nature, and the application of even higher resolution AFM mechanical analysis could indicate their function. These results support other works in the literature that clearly identify these upper parts of osteoderms as a unique calcified tissue [7,31].

The presence of the different calcified regions with different architectures prompted us to wonder what their mechanical properties would be and what would be their benefit for protection over the possibility of the whole osteoderm being formed from a single calcified structure. To evaluate this hypothesis, we initially set to determine the mechanical properties of the different regions of the osteoderm by nanoindentation. Our results showed that indeed, the three different calcified regions have a significant variation in their stiffness (Fig. 7), with the upper region being the stiffest, followed by the bone-like region and then the fibrous region. As expected, the region formed from bone presented a similar stiffness value to those reported in the literature for bone [43]. Interestingly, stiffness value of the upper calcified part is similar to the one observed for dentin [44]. This coincidence may imply a possible connection between the two tissues, even if they are present in completely different anatomical locations. Indeed, the literature includes works that suggest a connection between osteoderms and teeth [5].

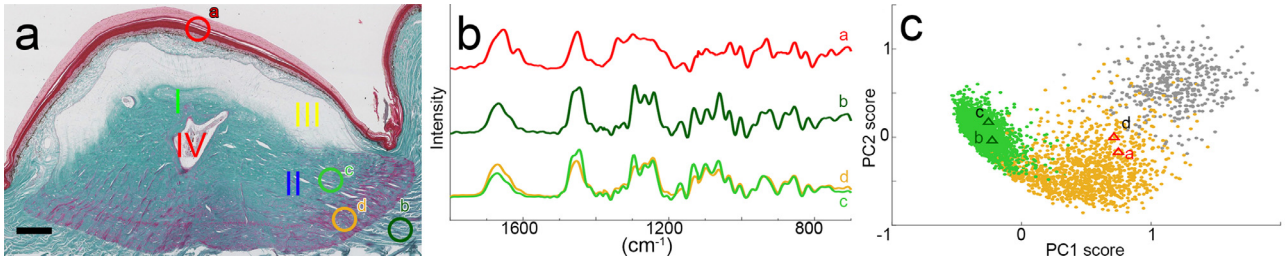

Fig. 4. (a) Optical micrograph of paraffin-embedded, 5-micron longitudinal section of osteoderm, stained with Masson's Trichrome. Scale bar = 100 µm. (b) Average Raman spectra of green and orange clusters (bottom row), in comparison with reference collagen spectrum (middle row) and reference keratin spectrum (top row) indicated by the circles with the respective colours in (a). (c) Principal component analysis (PCA) scores plot of Raman spectra measured in a rectangle area, as shown in Supplementary Fig. S4. The Raman spectra can be well-separated into three clusters, using hierarchical cluster analysis. Reference collagen spectra (dark green triangles) and keratin spectra (red triangles) are in the green and orange clusters, respectively. (For interpretation of the references to colour in this figure legend, the reader is referred to the web version of this article.)

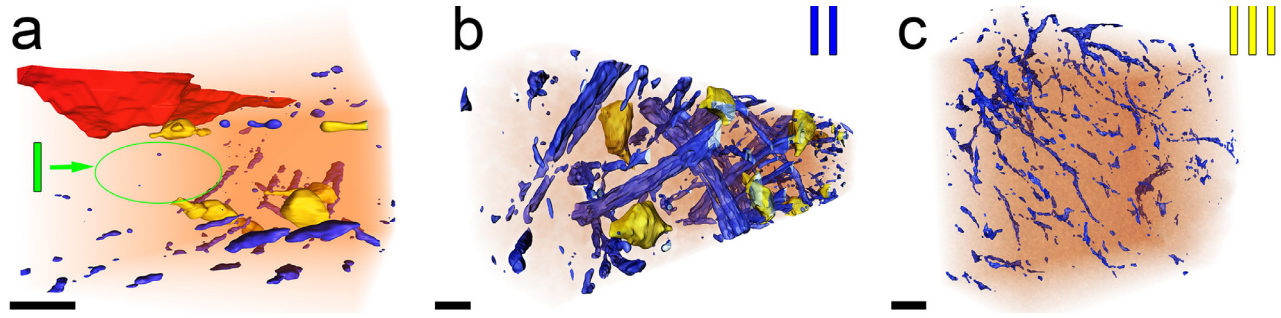

Fig. 5. Micro-CT scan 3D reconstruction of regions I, II and III of an osteoderm. (a) Micro-CT scan 3D reconstruction of region I (green arrow) indicates region highlighted (region inside green circle) between the vasculature (red) and region II (blue bundles), with vasculature in red, collagen bundles in blue, cells in yellow and mineral in light orange. Scale bar = 20 μm. (b) μ-CT scan 3D reconstruction of region II, with collagen bundles in blue, cells in yellow and mineral in orange. Scale bar = 5 μm. (c) μ-CT scan 3D reconstruction of region III, with collagen bundles in blue, cells in yellow and mineral in orange. Scale bar = 1 μm. (For interpretation of the references to colour in this figure legend, the reader is referred to the web version of this article.)

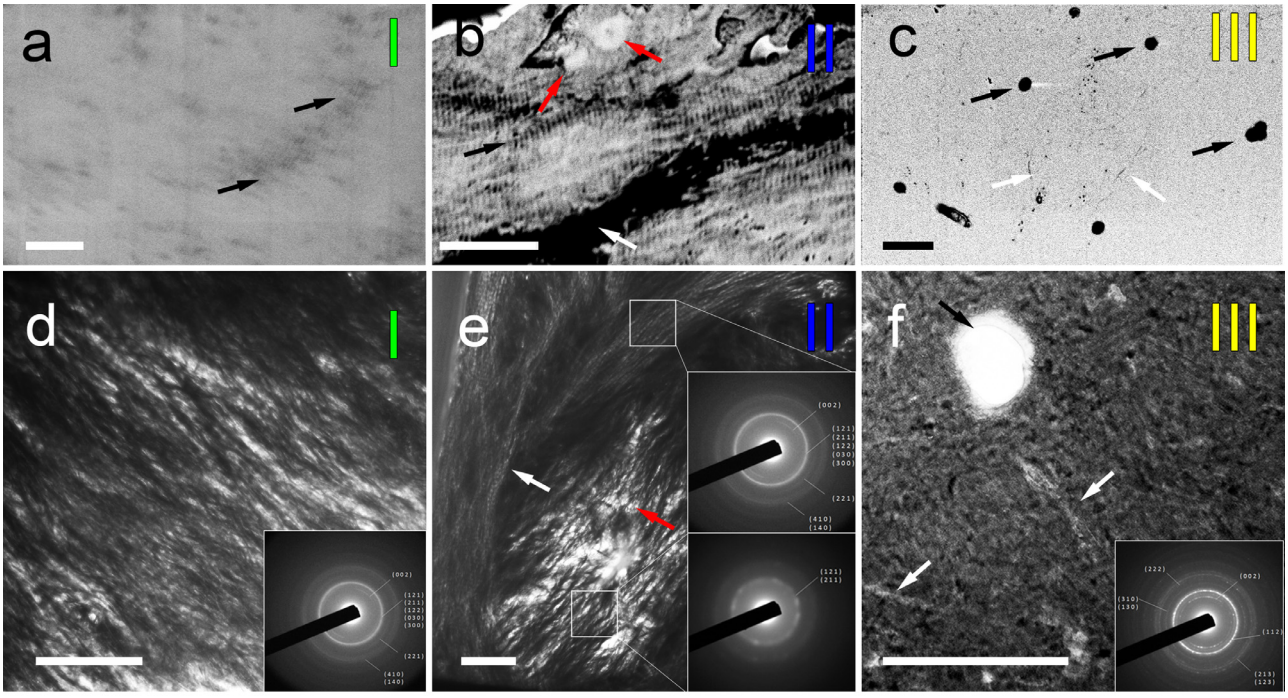

Fig. 6. Morphology and crystallinity of regions I, II and III in an osteoderm. (a) Backscattering scanning electron micrograph of a focused ion beam (FIB) section of region I, showing collagen fibres (arrow). Scale bar = 1 μm. (b) Backscattering scanning electron micrograph of a FIB section of region II, showing collagen fibres (black arrows), dense spheroids (red arrows) and a non-mineralized region (white arrow). Scale bar = 1 μm. (c) Backscattering scanning electron micrograph of a FIB section of region III, depicting microscopic fibres (black arrows) and nanofibres (white arrows). Scale bar = 1 μm. (d) TEM and electron diffraction image (inset) of region I. (e) TEM and electron diffraction images (inset) of region II. (f) TEM and electron diffraction image (inset) of region III. Scale bars = 0.5 μm. (For interpretation of the references to colour in this figure legend, the reader is referred to the web version of this article.)

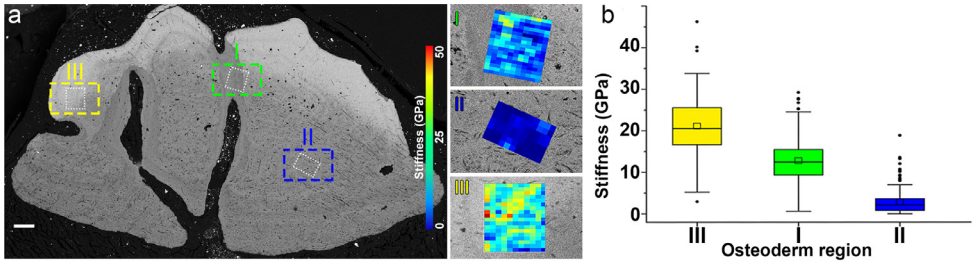

Fig. 7. Mechanical properties of the three regions in osteoderms. (a) Stiffness maps, obtained by nano-indentation tests using an atomic force microscope, are overlaid with a scanning electron micrograph of an osteoderm. The areas where nano-indentations were performed are indicated by dashed rectangles. Stiffness patterns of the three regions (I, II, II) are shown. (b) Bar plot of stiffness maps for the three regions indicated in (a). The standard deviation is presented along with boxes where the top and bottom of each box represent the 75th and 25th percentiles, respectively, and the inside line corresponds to the median. The filled square denotes the mean, and whiskers show the range of outer-most data points that fall within the 1.5 × interquartile range.

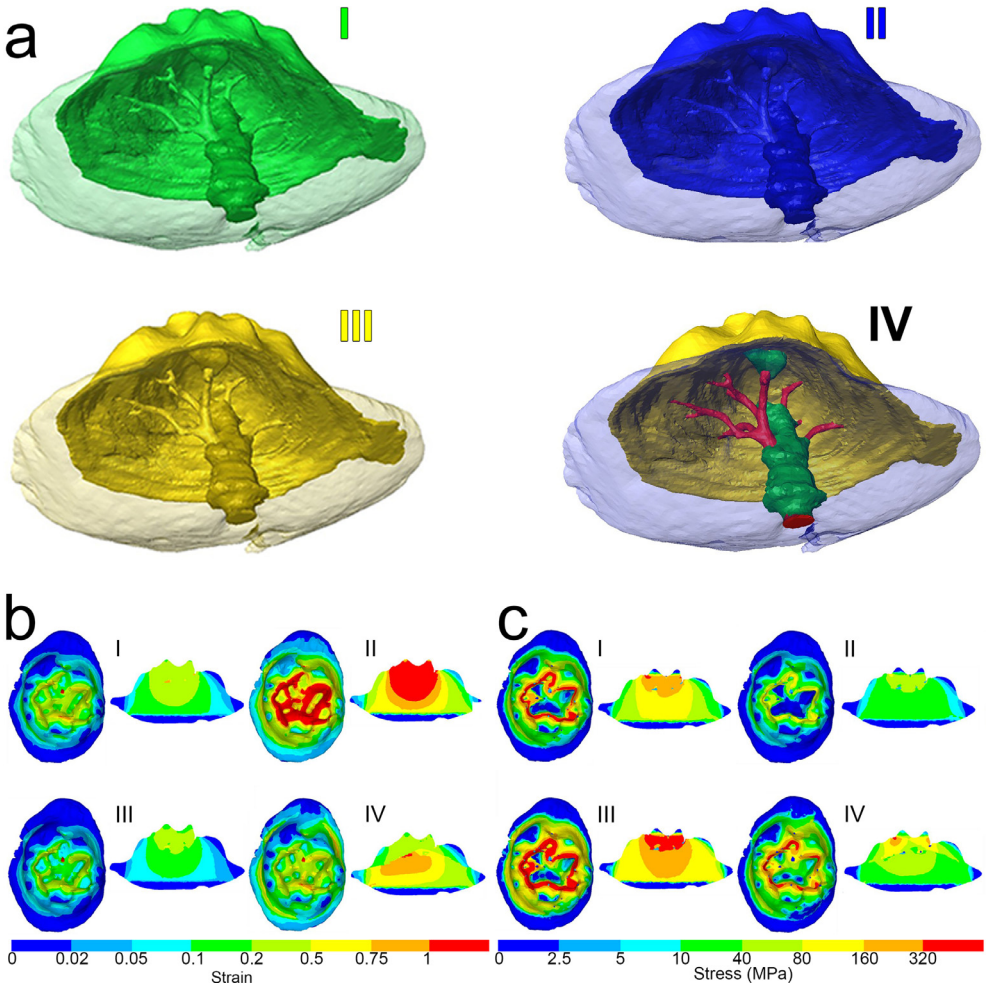

Fig. 8. Mechanical simulation of osteoderms. (a) Four mechanical loading scenarios were simulated by finite element modelling and assuming the stiffness values measured by AFM (Fig. 7) for the reconstructed osteoderm (aI, aII and aIII) and real osteoderm aIV, obtained from CT scan data. (b) and (c) Distribution of strain (%) and stress under application of force (b) or displacement (c) obtained by finite element analysis of a 3D model of the osteoderm, indicating large variation in stress and strain for different scenarios. (For interpretation of the references to colour in this figure legend, the reader is referred to the web version of this article.)

Once again, these results corroborate the literature, with the addition that the internal regions of the osteoderm may be divided into two subregions with significant variation in stiffness. This refinement to the description of osteoderm characteristics, probably would not have any impact on previous measurements and simulations [4,22,23], since the bulk of the osteoderm can be approximated to just two calcified regions: the upper dense part and the fibrous region.

Having measured stiffness of the different calcified regions, we set out to simulate (Fig. 8(a)) the contribution of each distinct calcified region to the overall mechanical performance of the whole osteoderm as load bearer for the animal. We also asked whether the combination of the different calcified regions would outperform a theoretical osteoderm formed from a single calcified tissue, since the latter is the case for bone.

Our simulation results show that osteoderms are damage-tolerant structures that can resist the application of external forces (Fig. 8). Moreover, our results show that if osteoderms were formed by a single tissue, they would not provide the desired protection to the animal. Indeed, our simulation suggests that if osteoderms were formed only from either bone (Fig. 8(aI)) or the dense calcified region (Fig. 8(aIII)), the osteoderm can robustly response to the application of external forces with generation of low levels of strains (Fig 8(bI&III)). However, considering these two stiff mechanical properties and under the application of external displacement the osteoderm exhibit large levels of stresses (Fig. 8(c I&III)) which may lead to failure. Moreover, if the osteoderm were formed only from the fibrous region (Fig. 8(aII)), while under application of strains osteoderm shows small levels of stresses, application of stress lead to generation of large strains that may lead to complete collapse. Taken together, the simulation results suggest that the most robust way to avoid the mechanical failure of the osteoderm (Fig. 8(b), (c) IV) is to combine the three different calcified regions we have identified here (Fig. 8(aIV)), which is indeed the way the osteoderms of *Heloderma suspectum* are found in nature.

Drawing an analogy between an osteoderm and a full medieval armour [46,47], the external metal layer would be represented by region III and the internal soft padding would be represented by region II, in addition to a special reinforcement, represented by region I, that protects delicate internal structures (for example, the vasculature).

5. Conclusions

In this work, we demonstrated using several nano-micro analytical methods that osteoderms from *Heloderma suspectum* are formed from three calcified regions with distinct nano architecture and with slightly different organic composition. Using AFM

and computational simulation, we also demonstrated that these distinct calcified regions present different mechanical properties, which when combined, provide the best load bearing mechanism to the animal.

This protective function of the osteoderm is, according to our results, likely to stem from its nano architecture. Our results suggest that different hard tissues indeed present different nano architectures, as is widely known from the differences in bone and teeth. Therefore, one important question raised by our results is whether there are other hard tissues in vertebrates, such as the sclerotic rings, or the chameleon's tongue-bone, which might also present different nano architectures associated to their functions? Another question also raised is whether such distinct nano architecture might have been created by different kinds of cells, other than the ones (such as osteoblasts) commonly known as responsible for the synthesis of hard tissues.

Finally, we believe this study has contributed towards a better knowledge of the structure-function relationship of these hierarchical structures, which might in turn provide a source of inspiration for the design of bioinspired and biomimetic materials.

Declaration of Competing Interest

The authors declare that they have no known competing financial interests or personal relationships that could have appeared to influence the work reported in this paper.

Acknowledgments

We would like to thank M. Stiefel for the discussion about FIB sample preparation and the Pathology Laboratory, Zoological Society of London for the donation of material to the Evans Lab. EM and YJ are grateful for funding from Cancer Research UK [C57744/A22057] and the Leverhulme Trust (RPG-2018-443). We would like thank Gabriel Ugueto for drawing the illustrations of lizards and osteoderms.

Supplementary materials

Supplementary material associated with this article can be found, in the online version, at doi:10.1016/j.actbio.2020.02.029.

References

[1] I.H. Chen, W. Yang, M.A. Meyers, Leatherback sea turtle shell: a tough and flexible biological design, Acta Biomater. 28 (2015) 2–12.
[2] R.V. Hill, Integration of morphological data sets for phylogenetic analysis of amniota: the importance of integumentary characters and increased taxonomic sampling, Syst. Biol. 54 (4) (2005) 530–547.
[3] M.K. Vickaryous, B.K. Hall, Development of the dermal skeleton in alligator mississippiensis (Archosauria, crocodylia) with comments on the homology of osteoderms, J Morphol. 269 (4) (2008) 398–422.
[4] I.H. Chen, W. Yang, M.A. Meyers, Alligator osteoderms: mechanical behavior and hierarchical structure, Mater. Sci. Eng. C Mater. Biol. Appl. 35 (2014) 441–448.
[5] M.K. Vickaryous, J.Y. Sire, The integumentary skeleton of tetrapods: origin, evolution, and development, J. Anat. 214 (4) (2009) 441–464.
[6] R. Ruibal, V. Shoemaker, Osteoderms in anurans, J. Herpetol. 18 (3) (1984) 313–328.
[7] M.K. Vickaryous, G. Meldrum, A.P. Russell, Armored geckos: a histological investigation of osteoderm development in Tarentola (Phyllodactylidae) and Gekko (Gekkonidae) with comments on their regeneration and inferred function, J. Morphol. 276 (11) (2015) 1345–1357.
[8] M.L. Moss, Comparative histology of dermal sclerifications in reptiles, Acta Anat. 73 (4) (1969) 510.
[9] M.K. Vickaryous, B.K. Hall, Osteoderm morphology and development in the nine-banded armadillo, Dasypus novemcinctus (Mammalia, Xenarthra, Cingulata), J. Morphol. 267 (11) (2006) 1273–1283.
[10] G.O. Cherepanov, Nature of the turtle shell: morphogenetic causes of bone variability and its evolutionary implication, Paleontol. J. 50 (14) (2016) 1641–1648.
[11] J.Y. Sire, P.C. Donoghue, M.K. Vickaryous, Origin and evolution of the integumentary skeleton in non-tetrapod vertebrates, J. Anat. 214 (4) (2009) 409–440.
[12] J.I. Mead, B.W. Schubert, S.C. Wallace, S.L. Swift, Helodermatid lizard from the mio-pliocene oak-hickory forest of Tennessee, eastern USA, and a review of Monstersaurian Osteoderms, Acta Palaeontol. Pol. 57 (1) (2012) 111–121 11.
[13] R. Hoffstetter, Observations sur les ostéodermes et la classification des anguidés actuels et fossiles (Reptiles, Sauriens), Bull. Muséum Natl. d'hist. Naturell. 34 (1962) 149–157.
[14] C.Y. Sun, P.Y. Chen, Structural design and mechanical behavior of alligator (Alligator mississippiensis) osteoderms, Acta Biomater. 9 (11) (2013) 9049–9064.
[15] F. Clarac, A. Quilhac, The crocodylian skull and osteoderms: a functional exaptation to ectothermy? Zoology 132 (2019) 31–40.
[16] T. Owerkowicz, Heat transfer through skin with and without osteoderms in the American alligator, FASEB J 30 (1_supplement) (2016) S15.3–S15.3.
[17] J.O. Farlow, S. Hayashi, G.J. Tattersall, Internal vascularity of the dermal plates of Stegosaurus (Ornithischia, Thyreophora), Swiss J. Geosci. 103 (2) (2010) 173–185.
[18] M.R. Seidel, The osteoderms of the American alligator and their functional significance, Herpetologica 35 (4) (1979) 375–380.
[19] F. Clarac, V. De Buffrénil, J. Cubo, A. Quilhac, Vascularization in ornamented osteoderms: physiological implications in ectothermy and amphibious lifestyle in the crocodylomorphs? Anat. Rec. 301 (1) (2018) 175–183.
[20] C. Broeckhoven, A. du Plessis, C. Hui, Functional trade-off between strength and thermal capacity of dermal armor: insights from girdled lizards, J. Mech. Behav. Biomed. 74 (2017) 189–194.
[21] C. Dacke, R. Elsey, P. Trosclair, T. Sugiyama, J. Nevarez, M. Schweitzer, Alligator osteoderms as a source of labile calcium for eggshell formation, J. Zool. 297 (2015) 255–264.
[22] E. Frey, Das Tragsystem der Krokodile: Eine Biomechanische und Phylogenetische Analyse, Staatliches Museum fur Naturkunde, 1988.
[23] J.D. Currey, Mechanical properties and adaptations of some less familiar bony tissues, J. Mech. Behav. Biomed. Mater. 3 (5) (2010) 357–372.
[24] W. Yang, I.H. Chen, B. Gludovatz, E.A. Zimmermann, R.O. Ritchie, M.A. Meyers, Natural flexible dermal armor, Adv. Mater. 25 (1) (2013) 31–48.
[25] L.Z.A.J. Castanet, New data on the structure and the growth of the Osteoderms in the Reptile Anguis fagilis L. (Anguidae, Squamata), J. Morphol. 186 (1985) 327–342.
[26] V. Levrat-Calviac, L. Zylberberg, The structure of the osteoderms in the gekko: tarentola mauritanica, Am. J. Anat. 176 (4) (1986) 437–446.
[27] M.K. Vickaryous, B.K. Hall, Development of the dermal skeleton in alligator mississippiensis (Archosauria, Crocodylia) with comments on the homology of osteoderms, J. Morphol. 269 (4) (2008) 398–422.
[28] V.d. Buffrénil, J.-Y. Sire, J.-C. Rage, The histological structure of glyptosaurine osteoderms (Squamata: anguidae), and the problem of osteoderm development in squamates, J. Morphol. 271 (6) (2010) 729–737.
[29] C. Bochaton, V. De Buffrenil, M. Lemoine, S. Bailon, I. Ineich, Body location and tail regeneration effects on osteoderms morphology—are they useful tools for systematic, paleontology, and skeletochronology in diploglossine lizards (squamata, anguidae)? J. Morphol. 276 (11) (2015) 1333–1344.
[30] I.A. Cerda, J.B. Desojo, T.M. Scheyer, Novel data on aetosaur (Archosauria, Pseudosuchia) osteoderm microanatomy and histology: palaeobiological implications, Palaeontology 61 (5) (2018) 721–745.
[31] V. de Buffrénil, Y. Dauphin, J.-C. Rage, J.-Y. Sire, An enamel-like tissue, osteodermine, on the osteoderms of a fossil anguid (Glyptosaurinae) lizard, C. R. Palevol. 10 (5) (2011) 427–437.
[32] L. David T. S., Simon G., Osteoderms of elgaria panamintina MVZ 75918, 2018.
[33] J.A. Maisano, T.J. Laduc, C.J. Bell, D. Barber, The cephalic osteoderms of varanus komodoensis as revealed by high-resolution X-Ray computed tomography, Anat. Rec. 302 (10) (2019) 1675–1680.
[34] R.J. Laver, C.H. Morales, M.P. Heinicke, T. Gamble, K. Longoria, A.M. Bauer, J.D. Daza, The development of cephalic armor in the tokay gecko (Squamata: Gekkonidae: Gekko gecko), J. Morphol. 281 (2020) 213–228.
[35] D.J. Paluh, A.H. Griffing, A.M. Bauer, Sheddable armour: identification of osteoderms in the integument of Geckolepis maculata (Gekkota), Afr. J. Herpetol. 66 (1) (2017) 12–24.
[36] C. Florea, M. Dreucean, M.S. Laasanen, A. Halvari, Determination of young's modulus using AFM nanoindentation. Applications on bone structures, in: Proceedings of the 2011 E-Health and Bioengineering Conference (EHB), 2011, pp. 1–4.
[37] V. de Buffrénil, Y. Dauphin, J.-C. Rage, J.-Y. Sire, An enamel-like tissue, osteodermine, on the osteoderms of a fossil anguid (Glyptosaurinae) lizard, C. R. Palevol. 10 (5–6) (2011) 427–437.
[38] S. Bertazzo, E. Gentleman, K.L. Cloyd, A.H. Chester, M.H. Yacoub, M.M. Stevens, Nano-analytical electron microscopy reveals fundamental insights into human cardiovascular tissue calcification, Nat. Mater. 12 (6) (2013) 576–583.
[39] K. Rahunen, L. Rieppo, P. Lehenkari, M. Finnilä, S. Saarakkala, Evaluation of quantitativity of histological collagen stains in articular cartilage, Osteoarthr. Cartil. 24 (2016) S307–S308.
[40] C.R. Jacob, S. Luber, M. Reiher, Analysis of secondary structure effects on the IR and Raman spectra of polypeptides in terms of localized vibrations, J. Phys. Chem. B 113 (18) (2009) 6558–6573.
[41] D.J.S. Aubin, R.H. Stinson, J.R. Geraci, Aspects of the structure and composition of baleen, and some effects of exposure to petroleum hydrocarbons, Can. J. Zool. 62 (2) (1984) 193–198.
[42] D.J. Hulmes, Building collagen molecules, fibrils, and suprafibrillar structures, J. Struct. Biol. 137 (1–2) (2002) 2–10.
[43] K.E. Kadler, D.F. Holmes, J.A. Trotter, J.A. Chapman, Collagen fibril formation, Biochem. J. 316 (1) (1996) 1–11.

[44] X. Su, K. Sun, F.Z. Cui, W.J. Landis, Organization of apatite crystals in human woven bone, Bone 32 (2) (2003) 150–162.
[45] Y. Liu, D. Luo, T. Wang, Hierarchical structures of bone and bioinspired bone tissue engineering, Small 12 (34) (2016) 4611–4632.
[46] K. DeVries, R.D. Smith, Medieval Military Technology, University of Toronto Press, 2012.
[47] M.M.O. Art, B. Dean, Handbook of Arms and Armor, European and Oriental: Including the William H. Riggs Collection, Metropolitan Museum of Art, 1921.